Dioxygen Activation in Methane Monooxygenase: A Theoretical Study

Benjamin F. Gherman,[†] Mu-Hyun Baik,[†] Stephen J. Lippard,*[,‡] and Richard A. Friesner*[,†]

Contribution from the Department of Chemistry and Center for Biomolecular Simulation, Columbia University, New York, New York 10027, and Department of Chemistry, Massachusetts Institute of Technology, Cambridge, Massachusetts 02139

Received June 4, 2003; E-mail: rich@chem.columbia.edu

Abstract: Using broken-symmetry unrestricted Density Functional Theory, the mechanism of enzymatic dioxygen activation by the hydroxylase component of soluble methane monooxygenase (MMOH) is determined to atomic detail. After a thorough examination of mechanistic alternatives, an optimal pathway was identified. The diiron(II) state H_{red} reacts with dioxygen to give a ferromagnetically coupled diiron(II,III) $H_{superoxo}$ structure, which undergoes intersystem crossing to the antiferromagnetic surface and affords H_{peroxo}, a symmetric diiron(III) unit with a nonplanar μ-η^2:η^2-O_2^{2-} binding mode. Homolytic cleavage of the O—O bond yields the catalytically competent intermediate Q, which has a di (μ-oxo)diiron(IV) core. A carboxylate shift involving Glu243 is essential to the formation of the symmetric H_{peroxo} and Q structures. Both thermodynamic and kinetic features agree well with experimental data, and computed spin-exchange coupling constants are in accord with spectroscopic values. Evidence is presented for pH-independent decay of H_{red} and H_{peroxo}. Key electron-transfer steps that occur in the course of generating Q from H_{red} are also detailed and interpreted. In contrast to prior theoretical studies, a requisite large model has been employed, electron spins and couplings have been treated in a quantitative manner, potential energy surfaces have been extensively explored, and quantitative total energies have been determined along the reaction pathway.

Introduction

Soluble methane monooxygenase (sMMO) is a non-heme, diiron enzyme system found in methanotrophic bacteria that converts dioxygen and methane to alcohol and water.[1-3] Over the past years, extensive experimental and theoretical studies on the catalytic hydroxylation mechanism have been conducted, leading to substantial progress in understanding the mechanism at an atomic level of detail.[4-7] Although there is general agreement on the sequence of the major steps of the enzymatic reaction, considerable controversy remains concerning the structures and energetics of many of the intermediates and transition states in the catalytic cycle. The cycle consists of four principal species (Figure 1). The oxidized diiron(III) form H_{ox}, for which crystal structure data are available,[8-10] is the first
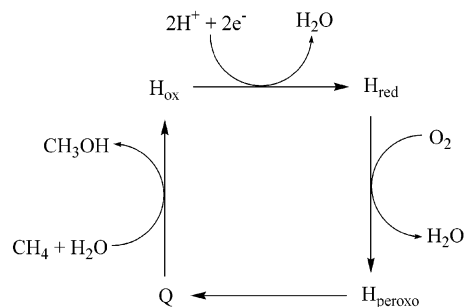

Figure 1. Overview of the MMOH catalytic cycle.

and represents the resting state of the sMMO hydroxylase (MMOH). Enzymatic catalysis is initiated when dioxygen reacts with the Fe(II) centers of the reduced form of MMOH (H_{red}) to give H_{peroxo}, a diiron(III) intermediate.[11-14] H_{peroxo} evolves to intermediate Q,[15] a diiron(IV) species,[14,16] which reacts with methane to yield methanol and H_{ox}.[17-21]

[†] Columbia University.
[‡] Massachusetts Institute of Technology.

(1) Hanson, R. S.; Hanson, T. E. *Microbiol. Rev.* **1996**, *60*, 439−471.
(2) Lipscomb, J. D. *Annu. Rev. Microbiol.* **1994**, *48*, 371−399.
(3) Liu, K. E.; Lippard, S. J. *Adv. Inorg. Chem.* **1995**, *42*, 263−289.
(4) Feig, A. L.; Lippard, S. J. *Chem. Rev.* **1994**, *94*, 759−805.
(5) Wallar, B. J.; Lipscomb, J. D. *Chem. Rev.* **1996**, *96*, 2625−2657.
(6) Merkx, M.; Kopp, D. A.; Sazinsky, M. H.; Blazyk, J. L.; Müller, J.; Lippard, S. J. *Angew. Chem., Int. Ed. Engl.* **2001**, *40*, 2782−2807.
(7) Baik, M.-H.; Newcomb, M.; Friesner, R. A.; Lippard, S. J. *Chem. Rev.* **2003**, *103*, 2385−2419.
(8) Rosenzweig, A. C.; Frederick, C. A.; Lippard, S. J.; Nordlund, P. *Nature* **1993**, *366*, 537−543.
(9) Rosenzweig, A. C.; Lippard, S. J. *Acc. Chem. Res.* **1994**, *27*, 229−236.
(10) Elango, N.; Radhakrishnan, R.; Froland, W. A.; Wallar, B. J.; Earhart, C. A.; Lipscomb, J. D.; Ohlendorf, D. H. *Protein Sci.* **1997**, *6*, 556−568.

(11) Liu, K. E.; Wang, D. L.; Huynh, B. H.; Edmondson, D. E.; Salifoglou, A.; Lippard, S. J. *J. Am. Chem. Soc.* **1994**, *116*, 7465−7466.
(12) Lee, S. K.; Nesheim, J. C.; Lipscomb, J. D. *J. Biol. Chem.* **1993**, *268*, 21 569−21 577.
(13) Brazeau, B. J.; Lipscomb, J. D. *Biochemistry* **2000**, *39*, 13 503−13 515.
(14) Liu, K. E.; Valentine, A. M.; Wang, D. L.; Huynh, B. H.; Edmondson, D. E.; Salifoglou, A.; Lippard, S. J. *J. Am. Chem. Soc.* **1995**, *117*, 10 174−10 185.
(15) Shu, L. J.; Nesheim, J. C.; Kauffmann, K.; Münck, E.; Lipscomb, J. D.; Que, L. *Science* **1997**, *275*, 515−518.
(16) Lee, S. K.; Fox, B. G.; Froland, W. A.; Lipscomb, J. D.; Münck, E. *J. Am. Chem. Soc.* **1993**, *115*, 6450−6451.

The present paper is focused on the dioxygen activation steps. We inquire as to how dioxygen is integrated into the diiron core of the MMOH active site to create a catalytically competent species, capable of inserting an oxygen atom into an aliphatic C−H bond at ambient temperature. We[22] and others[23−32] have addressed this question previously using quantum chemical methods. There is disagreement, however, about the dioxygen activation mechanism and the molecular structure of H_{peroxo}. A critical comparison between the different proposals has proved difficult owing to fundamentally different strategies and assumptions in constructing the computational models.[7]

The goal of the present study was therefore to examine in stringent detail the dioxygen activation mechanism using large computational models and quantum chemical methods capable of capturing the electronic structure of the MMOH catalytic species, both necessary (vide infra) features similar to those employed in our previous work.[22,33] The results allow us to comment on some controversial experimental findings, outlined in the next section, proposing explanations for the differences where possible. Advances in computing technology, as well as our own experience with the computational models,[34] have allowed us to investigate a significantly greater range of structures than were considered previously, in turn enabling a much more rigorous characterization of the dioxygen activation steps. The calculations are particularly demanding, because a large number of spin states exist at various points along the catalytic pathway. We have exhaustively enumerated these states and identified dominant reaction steps based on relative energies, taking into account whether particular transformations are spin-allowed.

Whereas our previous work considered only intermediates,[22] in this study we have also computed transition states, affording rate constants that can be compared with experimental data. These results can be used along with other criteria, such as consistency of computed structures with spectroscopic data for the intermediates and the thermodynamic stability of the various species, to assess the extent to which theory and experiment agree. This process is not simply a matter of judging theory based on its ability to predict experimental results. There are

uncertainties and controversies associated with many of the experiments as well, so that the entire process requires assembling a coherent, integrated picture in which both calculations and reported experimental data are critically examined. It is the case, however, that the high quality of the theoretical calculations with regard to system size, basis sets, and Density Functional Theory (DFT)[35] methodology, combined with the greatly expanded coverage of phase space with respect to both structural alternatives and spin couplings, enable such a picture to be assembled at a level of detail that has not been possible to date. Although we do not regard the results presented herein to be complete, the level of quantitative theory/experiment comparison has been substantially enhanced, which in turn increases confidence in the conclusions that are drawn.

Relevant Experimental Data. An extensive series of experiments has been performed on enzymes isolated from *Methylococcus capsulatus* (Bath) and *Methylosinus trichosporium* OB3b, hereafter MMO Bath and MMO OB3b, respectively, to determine the mechanism by which these bacteria oxidize methane. This body of work has established a number of important features that serve as benchmark points for our computational model.

The 'reactant' in the dioxygen activation process, the reduced form of MMOH (H_{red}), has EPR and zero-field Mössbauer spectra indicative of two high-spin iron(II) atoms that are weakly ferromagnetically (F) coupled and in different ligand environments.[36−39] X-ray crystallography, circular dichroism (CD) and magnetic circular dichroism (MCD) experiments reveal the iron atoms to be 5-coordinate, with the open coordination sites available for subsequent occupation by dioxygen-derived ligands.[40−42]

The first step of the catalysis is reaction of H_{red} with dioxygen. This process is poorly understood at present and many conflicting observations have been made. For example, the formation of H_{peroxo} was reported to be pH independent in the MMO Bath system,[14] whereas a different study using MMO OB3b found a sharp decrease in the H_{peroxo} formation rate with increasing pH.[43] The reported rate constants for the formation of H_{peroxo} are also different. When measured in the MMO OB3b system, H_{peroxo} formation had a rate constant of $9-12 \text{ s}^{-1}$ at 4 °C,[13] whereas rates of 25 s^{-1} and more recently $1-2 \text{ s}^{-1}$ have been found using MMO Bath.[11,14,44] Similarly puzzling is the observation that the decay rate of H_{red} is consistently higher than the rate of H_{peroxo} formation,[12,13,44,45] which could mean that there is at least one other species playing a role in the decay of H_{red}. However,

(17) Stirling, D. I.; Dalton, H. *Nature* **1981**, *291*, 169.
(18) Colby, J.; Stirling, D. I.; Dalton, H. *Biochem. J.* **1977**, *165*, 395−402.
(19) Fox, B. G.; Borneman, J. G.; Wackett, L. P.; Lipscomb, J. D. *Biochemistry* **1990**, *29*, 6419−6427.
(20) Andersson, K. K.; Froland, W. A.; Lee, S. K.; Lipscomb, J. D. *New J. Chem.* **1991**, *15*, 411−415.
(21) Rataj, M. J.; Kauth, J. E.; Donnelly, M. I. *J. Biol. Chem.* **1991**, *266*, 18 684−18 690.
(22) Dunietz, B. D.; Beachy, M. D.; Cao, Y. X.; Whittington, D. A.; Lippard, S. J.; Friesner, R. A. *J. Am. Chem. Soc.* **2000**, *122*, 2828−2839.
(23) Siegbahn, P. E. M.; Crabtree, R. H.; Nordlund, P. *J. Biol. Inorg. Chem.* **1998**, *3*, 314−317.
(24) Siegbahn, P. E. M. *Inorg. Chem.* **1999**, *38*, 2880−2889.
(25) Siegbahn, P. E. M. *J. Biol. Inorg. Chem.* **2001**, *6*, 27−45.
(26) Yoshizawa, K.; Hoffmann, R. *Inorg. Chem.* **1996**, *35*, 2409−2410.
(27) Yoshizawa, K.; Yokomichi, Y.; Shiota, Y.; Ohta, T.; Yamabe, T. *Chem. Lett.* **1997**, 587−588.
(28) Yoshizawa, K.; Yamabe, T.; Hoffmann, R. *New J. Chem.* **1997**, *21*, 151−161.
(29) Yoshizawa, K.; Ohta, T.; Yamabe, T.; Hoffmann, R. *J. Am. Chem. Soc.* **1997**, *119*, 12 311−12 321.
(30) Torrent, M.; Musaev, D. G.; Morokuma, K.; Basch, H. *J. Phys. Chem. B* **2001**, *105*, 4453−4463.
(31) Torrent, M.; Mogi, K.; Basch, H.; Musaev, D. G.; Morokuma, K. *J. Phys. Chem. B* **2001**, *105*, 8616−8628.
(32) Torrent, M.; Musaev, D. G.; Basch, H.; Morokuma, K. *J. Comput. Chem.* **2002**, *23*, 59−76.
(33) Gherman, B. F.; Dunietz, B. D.; Whittington, D. A.; Lippard, S. J.; Friesner, R. A. *J. Am. Chem. Soc.* **2001**, *123*, 3836−3837.
(34) Friesner, R. A.; Baik, M.-H.; Guallar, V.; Gherman, B. F.; Wirstam, M.; Murphy, R. B.; Lippard, S. J. *Coord. Chem. Rev.* **2003**, *238−239*, 267−290.

(35) Parr, R. G.; Yang, W. *Density Functional Theory of Atoms and Molecules*; Oxford University Press: New York, 1989.
(36) Dewitt, J. G.; Bentsen, J. G.; Rosenzweig, A. C.; Hedman, B.; Green, J.; Pilkington, S.; Papaefthymiou, G. C.; Dalton, H.; Hodgson, K. O.; Lippard, S. J. *J. Am. Chem. Soc.* **1991**, *113*, 9219−9235.
(37) Fox, B. G.; Surerus, K. K.; Münck, E.; Lipscomb, J. D. *J. Biol. Chem.* **1988**, *263*, 10 553−10 556.
(38) Fox, B. G.; Hendrich, M. P.; Surerus, K. K.; Andersson, K. K.; Froland, W. A.; Lipscomb, J. D.; Münck, E. *J. Am. Chem. Soc.* **1993**, *115*, 3688−3701.
(39) Hendrich, M. P.; Münck, E.; Fox, B. G.; Lipscomb, J. D. *J. Am. Chem. Soc.* **1990**, *112*, 5861−5865.
(40) Pulver, S.; Froland, W. A.; Fox, B. G.; Lipscomb, J. D.; Solomon, E. I. *J. Am. Chem. Soc.* **1993**, *115*, 12 409−12 422.
(41) Rosenzweig, A. C.; Nordlund, P.; Takahara, P. M.; Frederick, C. A.; Lippard, S. J. *Chem. Biol.* **1995**, *2*, 409−418.
(42) Whittington, D. A.; Lippard, S. J. *J. Am. Chem. Soc.* **2001**, *123*, 827−838.
(43) Lee, S. K.; Lipscomb, J. D. *Biochemistry* **1999**, *38*, 4423−4432.
(44) Valentine, A. M.; Stahl, S. S.; Lippard, S. J. *J. Am. Chem. Soc.* **1999**, *121*, 3876−3887.
(45) Liu, Y.; Nesheim, J. C.; Lee, S. K.; Lipscomb, J. D. *J. Biol. Chem.* **1995**, *270*, 24 662−24 665.

no positive identification of such an intermediate has been made to date and its existence is mainly supported by the rate mismatch between H_{red} decay and H_{peroxo} formation. There are also a number of features that have been fairly well established. H_{peroxo} has consistently been the first directly observable intermediate following the decay of H_{red}.[11-14,16] Mössbauer studies suggest that H_{peroxo} is diamagnetic owing to antiferromagnetic (AF) coupling of the two iron atoms.[11,14] A comparison with spectroscopic data from structurally well-defined Fe(III) peroxide model complexes[46-49] point to two electronically equivalent high-spin Fe(III) atoms that are symmetrically bridged by the peroxo moiety. Whether the peroxide group adopts an end-on, a $\mu\text{-}\eta^1:\eta^1$, or a $\mu\text{-}\eta^2:\eta^2$ coordination geometry could not be resolved, however. An oxygen kinetic isotope effect (KIE) of 1.016 ($^{16}O^{16}O$ vs $^{18}O^{16}O$), determined for steady-state turnover,[50] indicates that the O−O bond order decreases substantially at the rate-limiting transformation.

The last step of the catalytic cycle that we consider in this work is decay of H_{peroxo} to form Q. Although there is no doubt that the two intermediates are directly connected, the decay rate of H_{peroxo} matching the formation rate of Q,[14,43] there is disagreement in the literature on the actual rate. In the MMO OB3b system, a rate constant k_{obs} of 2.4 s^{-1} at 4 °C and pH 7 was measured.[13] In the same work, it was found that the rate decreases sharply with increasing pH. In a different study using MMO Bath, however, H_{peroxo} decay had a rate constant of 0.45 s^{-1} at 4 °C and was independent of pH in the range 6.6 ≤ pH ≤ 8.6.[14] Spectroscopic data do concur that Q contains two nearly equivalent high-valent Fe(IV) atoms that are AF-coupled.[11,14-16]

Computational Methods

All calculations were carried out with the Jaguar v4.1 suite of ab initio quantum chemistry programs.[51,52] The B3LYP functional[53-55] was used for all DFT calculations. To model correctly the open shell orbitals on the high-spin iron atoms in MMOH, an unrestricted DFT (UDFT) methodology was utilized. AF-coupling was achieved through the use of broken symmetry (BS) UDFT wave functions.[56] We have discussed the use of this approximation in the context of MMOH modeling in previous work.[22] Although the BS/UDFT methodology is not a completely rigorous treatment of the diiron spin manifold, it has proved to be a very useful and practical approximation, providing a substantial increase in realism as compared to simpler approaches, which typically employ F-coupling for all species.

The starting model used in this study contains ∼100 atoms of the reduced MMOH active site taken from the coordinates in ref 41 (Figure 2). As compared to smaller models, this large model is critical[22] to maintaining key structural features seen in the crystallographic data[8,41,57] and therefore in retaining biological relevance. Geometry optimizations
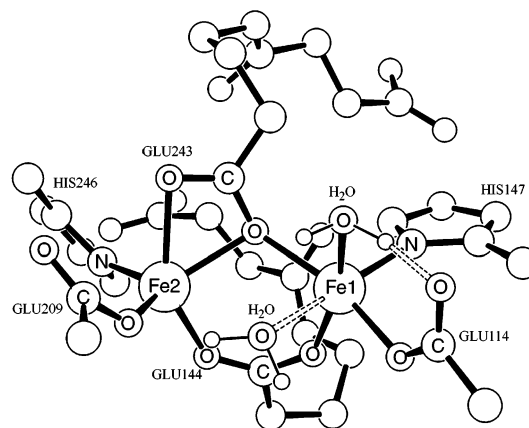

Figure 2. Reduced MMOH crystal structure, adapted from ref 41. Only residues coordinated to the iron atoms are labeled. Hydrogen atoms on the protein residues are omitted for clarity.

were carried out with the 6-31G basis set, except for the inclusion of polarization functions (i.e., the 6-31G** basis set) on selected atoms near the dinuclear iron core. The Los Alamos LACVP** basis set,[58-60] with an effective core potential and polarization functions, was used for the two iron atoms. To obtain accurate relative energies of qualitatively different structures, single-point calculations were performed on the optimized geometries. For atoms near the diiron core, the cc-pVTZ(-f) basis set of Dunning[61] was used in these calculations, whereas the 6-31G** basis was applied to atoms on the periphery of the model. The iron atoms were treated with the LACV3P** basis set, a triple-ζ quality basis compatible with the Fe effective core potential.[58-60]

Mappings of energy surfaces, performed along every reaction coordinate in the study, were achieved by freezing one or more coordinates at different values and optimizing all other degrees of freedom. All mappings were performed with the small mixed basis set. Use of the large mixed basis set in this case significantly increases computational time, but only minimally affects relative energies along the reaction coordinates.[33] Energetic maxima along the reaction coordinates were then used as starting structures for transition state searches, which were carried out using the quadratic synchronous transit (QST) method.[62] In this approach, the initial part of the transition state search is restricted to a circular curve connecting the reactant, transition state guess, and product, after which the optimizer follows the Hessian eigenvector most similar to the tangent of the circular curve.

Vibrational frequencies were calculated analytically. Due to the expense of these calculations, the full MMOH model (Figure 2) was truncated to approximately 40−45 atoms (Figure 3), which decreased the cost of the frequency calculations by roughly 90%. Glutamate residues coordinated to the iron atoms were cut between C_α and C_β, and capped with hydrogen atoms. Histidine residues were replaced by NH_3 ligands. The positions of the capping carboxylate and ammonia hydrogen atoms were then optimized with the structure otherwise frozen, and the results were used for the frequency calculation. From the frequency calculations, zero point energy corrections as well as enthalpy and entropy corrections can be obtained, thereby allowing free energy differences at room temperature to be calculated for all reactions.

Mulliken spin density analysis has become a routine tool to confirm that a reasonable electronic structure has been reached.[7,34] In addition, it provides a convenient method of tracing electron flow. By definition,

(46) Micklitz, W.; Bott, S. G.; Bentsen, J. G.; Lippard, S. J. *J. Am. Chem. Soc.* **1989**, *111*, 372−374.
(47) Menage, S.; Brennan, B. A.; Juarezgarcia, C.; Munck, E.; Que, L. *J. Am. Chem. Soc.* **1990**, *112*, 6423−6425.
(48) Brennan, B. A.; Chen, Q. H.; Juarezgarcia, C.; True, A. E.; Oconnor, C. J.; Que, L. *Inorg. Chem.* **1991**, *30*, 1937−1943.
(49) Kim, K.; Lippard, S. J. *J. Am. Chem. Soc.* **1996**, *118*, 4914−4915.
(50) Stahl, S. S.; Francisco, W. A.; Merkx, M.; Klinman, J. P.; Lippard, S. J. *J. Biol. Chem.* **2001**, *276*, 4549−4553.
(51) Jaguar v4.1, Schrödinger, Inc., Portland, Oregon, 2000.
(52) Friesner, R. A.; Murphy, R. B.; Beachy, M. D.; Ringnalda, M. N.; Pollard, W. T.; Dunietz, B. D.; Cao, Y. X. *J. Phys. Chem. A* **1999**, *103*, 1913−1928.
(53) Johnson, B. G.; Gill, P. M. W.; Pople, J. A. *J. Chem. Phys.* **1993**, *98*, 5612−5626.
(54) Becke, A. D. *J. Chem. Phys.* **1993**, *98*, 1372−1377.
(55) Lee, C. T.; Yang, W. T.; Parr, R. G. *Phys. Rev. B* **1988**, *37*, 785−789.
(56) Noodleman, L. *J. Chem. Phys.* **1981**, *74*, 5737−5743.

(57) Rosenzweig, A. C.; Brandstetter, H.; Whittington, D. A.; Nordlund, P.; Lippard, S. J.; Frederick, C. A. *Proteins: Struct., Funct., Genet.* **1997**, *29*, 141−152.
(58) Hay, P. J.; Wadt, W. R. *J. Chem. Phys.* **1985**, *82*, 270−283.
(59) Wadt, W. R.; Hay, P. J. *J. Chem. Phys.* **1985**, *82*, 284−298.
(60) Hay, P. J.; Wadt, W. R. *J. Chem. Phys.* **1985**, *82*, 299−310.
(61) Dunning, T. H. *J. Chem. Phys.* **1989**, *90*, 1007−1023.
(62) Peng, C. Y.; Schlegel, H. B. *Isr. J. Chem.* **1993**, *33*, 449−454.
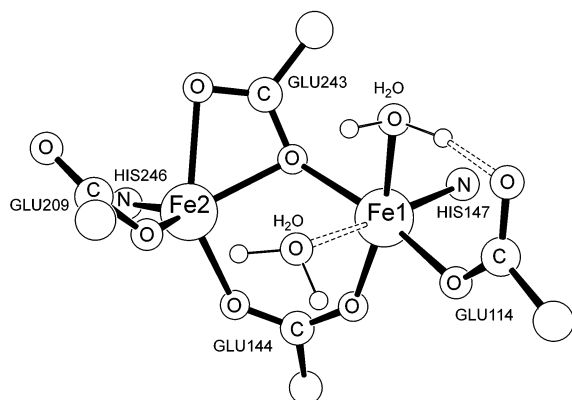
Figure 3. Truncated H_{red} model. Only residues coordinated to the iron atoms are labeled. Hydrogen atoms on the protein residues are omitted for clarity.

α-electrons are assigned positive spin and β-electrons negative spin. In principle, one would expect a spin density of 4.0 for each Fe(II)-center in H_{red} owing to the four unpaired electrons in a high-spin d^6 configuration. Due to electronic metal−ligand interactions and the intrinsic formalism of assigning electrons to a specific atom, however, noninteger spin densities lower than the ideal number are commonly observed. A spin density of 3.5−3.7, for example, is a typical signature for a high-spin Fe(II)-d^4 center, whereas a spin density of 3.8−4.1 indicates an Fe(III)-d^5 center.

Results

A. Reduced Enzyme H_{red} and Preparation for Attack by Dioxygen. The diiron(II) state was modeled with high-spin $S = 2$, F-coupled iron atoms in accord with experimental evidence,[14,36−39] giving a ^9A state, H_{red}−F. The case of AF-coupling, i.e., the ^1A state H_{red}−AF, is discussed in the Supporting Information (text section A). As in the crystal structure,[41,42] geometry optimization maintained a loosely coordinated water molecule, trans to the histidine coordinated to Fe1. The optimized model had an Fe−Fe distance about 0.35 Å longer than in the crystal structure, reflecting the energetically flat Fe−Fe potential surface, an issue discussed previously in ref 22. The discrepancy in distance may reflect relatively subtle errors in the DFT functional, but has a minimal effect on the major structural and energetic features of the reaction chemistry discussed below. In fact, the energy change as a function of this coordinate, over the relevant range of distances, is extremely small, on the order of 1−2 kcal/mol at most.

The first step in the reaction of H_{red} with O_2 involves departure of the loosely coordinated water molecule trans to the histidines. Figure S2 depicts the reaction coordinate for this process, which is energetically uphill while the water molecule remains in the vicinity of the diiron core. As the water moves away from the core, increasing entropy lowers the system free energy. Computation of the final free energy change upon departure of the water involves the summation of various energy components. First, if the water molecule is considered to be released into the gas phase, ΔH for $H_{red} \rightarrow H_{red}$-primed + $H_2O_{(g)}$ is +16.39 kcal/mol, including zero-point energy and enthalpy corrections at 25 °C. In reality, however, the water molecule is released into solution, and the gas phase-to-solution free energy of transfer for this process must also be included. The enthalpy change for $H_{red} \rightarrow H_{red}$-primed + $H_2O_{(aq)}$ then becomes +8.92 kcal/mol.[63,64] Second, when the water molecule departs the

protein environment for solution, van der Waals interactions with the protein are lost at a cost of approximately 6 kcal/mol.[65] This correction is necessary because DFT methods do not account for vdW interactions,[66,67] which would lead to a serious error for the energy of the water-containing species (i.e., H_{red}). The final enthalpy change is then +14.92 kcal/mol.[64] The entropic correction (the translational/rotational entropy gain) for release of the water molecule is significant, 13.09 kcal/mol. The final free energy change is therefore +1.83 kcal/mol, and the reaction is thus nearly isoenergetic. The spin and charge distributions (Table S10) are only slightly different from those seen for H_{red}. The H_{red}-primed structure created by the loss of the water molecule has open coordination sites on Fe1 and Fe2, each being 5-coordinate, which are available for dioxygen binding in the next steps of the reaction.

B. Attack of Dioxygen and Formation of the Peroxo Intermediate H_{peroxo}. B.1. Overview. The next step in reductive activation of dioxygen is for O_2 to enter the enzyme active site, bind to the diiron core, and form H_{peroxo}. There has been some controversy as to whether there are stable intermediates prior to H_{peroxo}. Our calculations address this question in what follows.

The attack of dioxygen upon the diiron core is complicated by several important issues: (1) One or two electrons can be transferred from the diiron core to dioxygen, forming superoxo and peroxo moieties, respectively. Furthermore, these transfers can take place at different points along the reaction coordinate. (2) There are a number of different possible $H_{superoxo}$ or H_{peroxo} structures. (3) There are a large number of possible ways to couple the spins on the oxygen atoms of dioxygen with the spins on the two iron atoms.

We have addressed these three issues by modeling the various relevant alternatives, comparing the activation free energies of the possible kinetic pathways as well as assessing whether they would be spin-forbidden, which would diminish the effective rate constant substantially. The optimal pathway is then selected based on energetic and spin compatibility considerations (Supporting Information text sections C and D). Here, we provide a brief overview of the manifold of structures and electronic states, and then focus on characterization of the optimal reaction pathway from both a qualitative and quantitative point of view.

B.2. $H_{superoxo}$ and H_{peroxo} Structures and Spin States. We begin our analysis by enumerating the $H_{superoxo}$ and H_{peroxo} structural/spin intermediates. These were generated by a series of computations employing different starting points, which in turn were based on the experimental data and physical/chemical intuition. All of these structures represent minima on the potential energy surface.

Three different $H_{superoxo}$ geometries, the cores of which are shown in Figure 4, were considered to be possibilities. $H_{superoxo}$-(a) was previously explored by us[22] and differs from

(63) The solvation energy of water has been computed using a continuum solvation model and amounts to 7.47 kcal/mol.
(64) The energetic corrections for solvation used here both for O_2(aq) and H_2O(aq) are solvation free energies. Adding these free energies of solvation to the computed enthalpies for the model systems is technically not appropriate and then creates a 'hybrid-energy' that is not ΔH in a rigorous sense. However, it is impossible to separate the free energy of solvation obtained from Henry's law or the continuum solvation model into an enthalpic and entropic term. For simplicity, we neglect this detail and use ΔH to denote the solvation-corrected enthalpy.
(65) Wirstam, M.; Lippard, S. J.; Friesner, R. A. *J. Am. Chem. Soc.* **2003**, *125*, 3980−3987.
(66) Kristyán, S.; Pulay, P. *Chem. Phys. Lett.* **1994**, *229*, 175−180.
(67) Pérez-Jordá, J. M.; Becke, A. D. *Chem. Phys. Lett.* **1995**, *233*, 134−137.
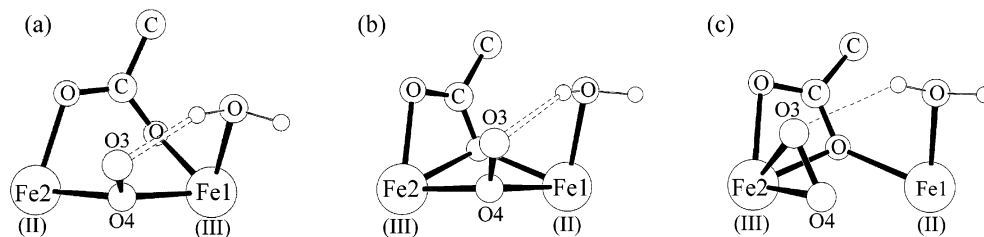
Figure 4. Three general possible geometries for $H_{superoxo}$. Only cores of the structures are shown. Dashed lines represent hydrogen bonds.
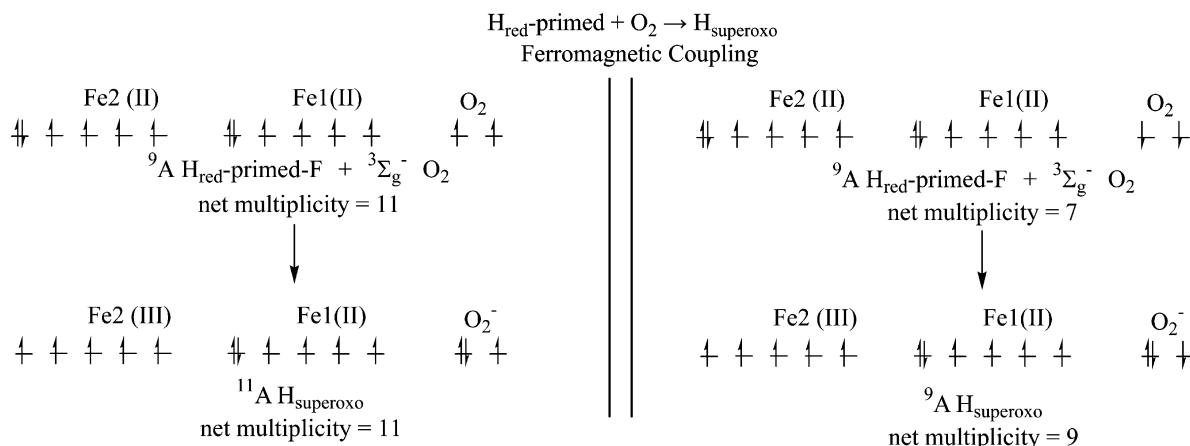
$$H_{red}\text{-primed} + O_2 \rightarrow H_{superoxo}$$
Ferromagnetic Coupling

Figure 5. Electron (d electrons for Fe1 and Fe2; π^* electrons for dioxygen) spins and couplings for the reaction of H_{red}-primed$-$F $+ O_2 \rightarrow H_{superoxo}-$F.

$H_{superoxo}$-(b) and $H_{superoxo}$-(c) by the positioning of Glu243. In each structure, stabilization of the O3$-$O4 superoxo ligand is provided either by a hydrogen bond to O3 (a and b) or by an Fe2$-$O3 bond accompanied by a weak O3-water interaction (c).

In principle, each of the above $H_{superoxo}$ structures can exist in a variety of electronic states. The two Fe(II) centers in H_{red}-primed-F give rise to a spin multiplicity of 9, with the 8 unpaired parallel spins taken to be spin up. As the triplet dioxygen approaches H_{red}-primed-F, its two unpaired electrons may both be aligned parallel or antiparallel to the electrons in H_{red}-primed-F (Figure 5). If the spins of the dioxygen-based electrons are parallel to those on the iron atoms, the total multiplicity of the system is 11. Oxidation of one of the iron atoms yields a $H_{superoxo}$ structure, which still has multiplicity of 11. We have determined that Fe2 is preferentially oxidized in $H_{superoxo}$ motifs (b) and (c) for all spin states considered (Tables S11, S12). If the two unpaired electrons on dioxygen are initially antiparallel to the spins in H_{red}-primed-F, then the net multiplicity of the combined system is 7. After Fe2 is oxidized and dioxygen reduced, the resulting $H_{superoxo}$ will have multiplicity 9 as illustrated in Figure 5. With reactants on the multiplicity 7 surface and products on the multiplicity 9 surface, intersystem crossing (ISC) must occur at some point along the reaction coordinate. In the AF-coupled case (Figure S3), a triplet or singlet $H_{superoxo}$ structure can be generated from the singlet H_{red}-primed-AF state in an analogous fashion to that for the multiplicity 11 and 9 F-coupled $H_{superoxo}$, respectively (Supporting Information text section B).

Core geometries of the two possible H_{peroxo} species are presented in Figure 6. The asymmetric H_{peroxo} structure was first presented elsewhere.[22] In the symmetric structure, Glu243 shifts so that O6 is hydrogen bonded to the water molecule coordinated to Fe1 rather than bridging the two iron atoms. The symmetric
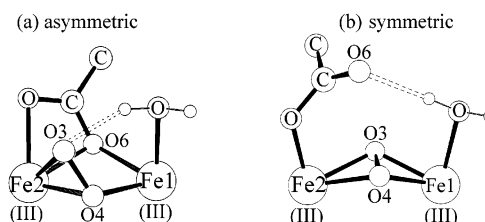

Figure 6. Two general possible geometries for H_{peroxo}. Only cores of the structures are shown. Dashed lines represent hydrogen bonds.

structure also has the peroxide moiety in a symmetric nonplanar bridging $\mu\text{-}\eta^2{:}\eta^2$ butterfly arrangement, similar to that which occurs following dioxygen activation by some dicopper complexes.[68−78] In each structure, stabilization is provided by a key hydrogen bond, whether it be O3-water in the asymmetric geometry or O6-water in the symmetric structure. The spin coupling alternatives for H_{peroxo} are considerably simpler than those for $H_{superoxo}$. The only unpaired electrons in the H_{peroxo} intermediate are the 5 d-electrons on each Fe(III) atom, which can F-couple to give a multiplicity of 11 or AF-couple to give a multiplicity of 1.

(68) Kitajima, N.; Morooka, Y. *J. Chem. Soc., Dalton Trans.* **1993**, 2665−2671.
(69) Kitajima, N.; Morooka, Y. *Chem. Rev.* **1994**, *94*, 737−757.
(70) Morooka, Y.; Fujisawa, K.; Kitajima, N. *Pure Appl. Chem.* **1995**, *67*, 241−248.
(71) Karlin, K. D.; Kaderli, S.; Zuberbuhler, A. D. *Acc. Chem. Res.* **1997**, *30*, 139−147.
(72) Liang, H. C.; Dahan, M.; Karlin, K. D. *Curr. Opin. Chem. Biol.* **1999**, *3*, 168−175.
(73) Siegbahn, P. E. M.; Wirstam, M. *J. Am. Chem. Soc.* **2001**, *123*, 11 819−11 820.
(74) Solomon, E. I.; Chen, P.; Metz, M.; Lee, S. K.; Palmer, A. E. *Angew. Chem. Int. Ed. Engl.* **2001**, *40*, 4570−4590.
(75) Que, L.; Tolman, W. B. *Angew. Chem., Int. Ed. Engl.* **2002**, *41*, 1114−1137.
(76) Metz, M.; Solomon, E. I. *J. Am. Chem. Soc.* **2001**, *123*, 4938−4950.
(77) Blackman, A. G.; Tolman, W. B. *Struct. Bond.* **2000**, *97*, 179−211.
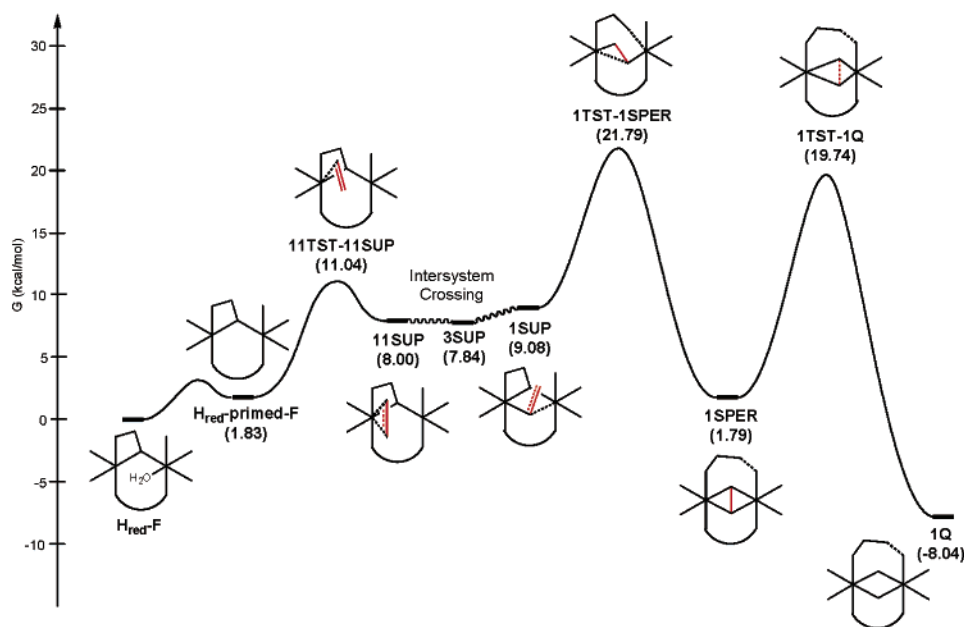(78) Mahadevan, V.; Gebbink, R. J. M. K.; Stack, T. D. P. *Curr. Opin. Chem. Biol.* **2000**, *4*, 228−234.

Figure 7. Schematic reaction energy profile for reductive dioxygen activation by MMOH.

Table 1. Relative Enthalpies, Entropies, and Free Energies (all at 25 °C) for the Alternative $H_{superoxo}$ and H_{peroxo} Structures

species	ΔH (kcal/mol)[a]	ΔS (cal/mol*K)	ΔG (kcal/mol)[a]
H_{red}-primed−F + O_2 (aq)	0.00	0.00	0.00
[9]A $H_{superoxo}$ (9SUP)	+0.27	−42.45	+12.93
[11]A $H_{superoxo}$ (11SUP)	−4.10	−34.43	+6.17
[1]A $H_{superoxo}$ (1SUP)	−5.61	−42.90	+7.18
[3]A $H_{superoxo}$ (3SUP)	−4.29	−34.31	+5.94
[11]A asymmetric H_{peroxo} (11APER)	−3.57	−45.08	+9.88
[11]A symmetric H_{peroxo} (11SPER)	−10.72	−42.80	+2.04
[1]A asymmetric H_{peroxo} (1APER)	−4.32	−50.21	+9.04
[1]A symmetric H_{peroxo} (1SPER)	−12.29	−46.26	−0.11

[a] Enthalpies and free energies include contributions from the solvation energy of O_2 and from the van der Waals interaction of O_2 with H_{red}-primed−F.

Table 1 summarizes these alternative intermediate structures and their total energies relative to H_{red}-primed-F. A number conclusions can be drawn immediately: (1) The lowest energy intermediate is the symmetric peroxo species **1SPER** (cf., Figure 6b), which is the only one that is comparable in energy to the starting complex. It will be expected to have significant population and hence be spectroscopically observable. We therefore identify species **1SPER** with H_{peroxo}. The suitability of species **1SPER** as a candidate for H_{peroxo} is further discussed below. (2) The absence of other low energy intermediates is consistent with the inability to detect any such species directly despite extensive experimental investigation of MMOH over the past decade. Some indirect evidence has led to speculation about the existence of other intermediates; we consider these arguments briefly in section A.1. of the Discussion section. Our calculations suggest that alternative explanations of these experiments are to be preferred. (3) Identification of species **1SPER** with H_{peroxo} leaves open the question of the optimal kinetic pathway to this state from the initial complex. Clearly there are a large number of alternatives, considering that one could pass through any of the states enumerated in Table 1. We have exhaustively investigated the various possible transition states for each putative process, and these results are presented in detail in the Supporting Information (text section C). The

Table 2. Relative Enthalpies, Entropies, and Free Energies (all at 25 °C) for the Species in Figure 8[a]

species	ΔH (kcal/mol)[b]	ΔS (cal/mol*K)	ΔG (kcal/mol)[b]
H_{red}−F + O_2 (aq)	0.00	0.00	0.00
H_{red}-primed−F + H_2O (aq) + O_2 (aq)	+14.92	+43.92	+1.83
11TST-11SUP	+13.35	+7.78	+11.04
11SUP	+10.82	+9.49	+8.00
3SUP	+10.63	+9.61	+7.84
1SUP	+9.31	+1.02	+9.08
1TST-1SPER	+22.41	+2.32	+21.79
1SPER	+2.68	+3.06	+1.79
1TST-1Q	+19.75	+0.10	+19.74
1MV-1Q	+11.14	−5.56	+12.82
1Q[c]	−7.93	+0.44	−8.04

[a] All intermediates and transition states from 11TST-11SUP onward include the energy for H2O (aq). [b] Enthalpies and free energies include contributions from the solvation energy of O_2 and from the van der Waals interaction of O_2 with H_{red}-primed-F. [c] Free energy does not include singlet stabilization energy arising from spin contamination considerations (see results section E).

optimal pathway, extracted from this analysis, is discussed in the next section.

B.3. Optimal Kinetic Pathway for the Formation of H_{peroxo}. The optimal kinetic pathway for the formation of H_{peroxo}, taking into account energetics and spin compatibility (Supporting Information text section D), is depicted in Figure 7. Relative energies for the states indicated in the Figure are listed in Table 2, and Mulliken spin densities are listed in Table 3. The structures labeled in Figure 7 are depicted with selected geometric information in Figure 8. The rate determining transition state is the species **1TST-1SPER**, in which the $H_{superoxo}$ species **1SUP** converts to H_{peroxo}.

The reaction coordinate for formation of the first intermediate in dioxygen activation, [11]A $H_{superoxo}$ (**11SUP**), is shown in Figure S7. Energy mapping for dioxygen approach along the [11]A surface reveals that the transition state (**11TST-11SUP**) occurs when O4 is 2.30−2.50 Å from the midpoint between the two iron atoms. The [11]A $H_{superoxo}$ that forms on this surface corresponds to a shallow minimum at an O4-diiron midpoint distance of ∼1.90 Å. To calculate free energies for these species,

Table 3. Mulliken Spin Densities for the Species in Figure 8

species	Fe1	Fe2	O3	O4
$H_{red}-F$	3.77	3.75	n/a	n/a
H_{red}-primed$-F$	3.75	3.73	n/a	n/a
11TST-11SUP	3.76	3.80	0.85	0.92
11SUP	3.70	3.89	0.78	0.79
3SUP	−3.76	3.92	0.75	0.75
1SUP	−3.75	4.04	−0.60	−0.23
1TST-1SPER	−3.92	4.00	−0.09	−0.29
1SPER	−4.02	4.00	−0.10	−0.09
1TST-1Q	−3.73	4.01	−0.25	−0.35
1MV-1Q	−3.13	3.86	−0.53	−0.67
1Q	−3.49	3.54	−0.06	−0.03

we estimate the van der Waals energy for dioxygen within the MMOH substrate binding cavity to be ∼6 kcal/mol,[65] an essential correction to the DFT energies of the dioxygen adducts. Second, since the final energy should reflect the equilibrium between dioxygen bound to the protein and O_2(aq), we account for the solubility of O_2 in water, which, from Henry's Law, is −3.95 kcal/mol at 25 °C. The transition state **11TST-11SUP** then has an enthalpy of 13.35 kcal/mol using the relative energy scale shown in Figure 7 and the entropy correction amounts to 7.78 eu with respect to $H_{red}-F$ and free dioxygen. It is interesting to note that the exchange of the water ligand with the dioxygen moiety in its superoxo form is entropically favorable, while being enthalpically uphill. Overall the free energy of activation is 11.04 kcal/mol.

The transition state geometry **11TST-11SUP** (Figure 8) has a slightly elongated (0.1 Å) Fe−Fe distance, a lengthened O3−O4 bond compared to 1.215 Å in dioxygen, and an Fe2−O3 bond that has formed to a notable extent at the transition state. Formation of an Fe2−O4 bond leads to $H_{superoxo}$ (**11SUP**), in which the O3−O4 bond has lengthened further. In both species, interaction with the water ligand bound to Fe1 and the bidentate binding of the superoxide moiety to Fe2 lead to energetic stabilization and indicate an advantage of side-on attack by dioxygen. End-on attack yields a structure with an unstable O3 atom directed outward from the diiron core. Crystal structures for H_{ox},[8–10,41,42] however, indicate there is water present in the substrate binding cavity which could possibly remain in the $H_{superoxo}$ intermediate and stabilize the superoxo moiety resulting from end-on dioxygen attack. Inclusion of such water molecules into the theoretical model will be undertaken in future QM/MM calculations.

ISC from the F to AF surface, facilitated by near energetic degeneracy as well as significant structural similarity, occurs next between **11SUP** and the ³A $H_{superoxo}$ structure **3SUP**. A second ISC to the energetically close ¹A $H_{superoxo}$ (**1SUP**) follows, corresponding to a spin flip of the one unpaired electron formally assigned to the superoxo moiety (Figure S3). **1SUP** has an Fe1−O4 bond, a shortened Fe2−O4 bond, and a decreased iron−iron distance. **1SUP** is stabilized by a hydrogen bond from O3 to the water ligand.

The free energy of activation versus **1SUP** to form the AF-coupled symmetric H_{peroxo} structure **1SPER** is +12.71 kcal/mol passing through the transition state **1TST-1SPER**, which has a relative free energy of +21.79 kcal/mol. The thermodynamic driving force ΔG for this reaction is −7.29 kcal/mol versus **1SUP** (Table 2) placing the H_{peroxo} species at a free energy of 1.79 kcal/mol on the relative energy scale shown in Figure 7. The reaction involves an initial shifting of Glu243 so

that O6 shifts from its bridging position between the two iron atoms. Glu243 then continues to move toward its final position in **1SPER,** where O6 forms a hydrogen bond to the water ligand on Fe1. Simultaneously, O3 rotates around the Fe2−O4 bond axis so as to occupy the bridging position formerly held by O6. The transition state (**1TST-1SPER**) reflects a geometry in which the Glu243 carboxylate shift and the rotation of O3 are both partially complete. This transition state is stabilized by a persistent weak interaction between O3 and the water ligand and by the early formation of an Fe2−O3 bond; the Fe1−O3 bond does not form until the reaction is nearly complete. The O3−O4 bond length is minimally changed at the transition state but becomes elongated by 0.15 Å to 1.478 Å, a typical peroxo distance, with formation of the μ-η^2:η^2 butterfly geometry.

C. Formation of Q from H_{peroxo}. The decay of **1SPER** to form intermediate Q, a di-(μ-oxo)diiron(IV) species, is facilitated by cleavage of the O3−O4 bond and contraction of the Fe−Fe distance. In the process, the O_2^{2-} peroxo moiety is formally reduced to two O^{2-} ions and each iron(III) is oxidized to iron(IV). The proposed mechanism involves homolytic cleavage of the oxygen−oxygen bond. The ¹A transition state **1TST-1Q**, $\Delta G^{\ddagger} = +17.95$ kcal/mol versus **1SPER** (Table 2), for this reaction (Figure 8) has already cleaved the O3−O4 bond by increasing this distance by 0.42 Å compared to that in **1SPER**. This process is accompanied by a 0.33 Å decrease in the Fe−Fe distance. Following this transition state, an unstable ¹A mixed-valent Fe(IV)Fe(III) state (**1MV-1Q**) can be identified with a free energy 6.92 kcal/mol lower than **1TST-1Q**. The Fe−Fe distance is decreased by another 0.32 Å and the O3−O4 distance is increased by another 0.35 Å in **1MV-1Q**. A related mixed-valent intermediate has been produced previously by cryoscopic reduction of intermediate Q and observed with Mössbauer spectroscopy.[79] With the oxidation of Fe1 complete, at this point the Fe1−O3 and Fe1−O4 bond lengths are ∼0.30 Å shorter than those for Fe2−O3 and Fe2−O4. The mixed-valent intermediate, with $\Delta G = +11.03$ kcal/mol versus **1SPER,** decays in an entirely downhill reaction to give intermediate Q (**1Q**). In this last step, the Fe−Fe distance shortens by 0.26 Å, the O3−O4 distance lengthens by 0.12 Å, and the Fe2-bridging oxygen distances decrease by about 0.2 Å. The **1Q** thus formed has both iron atoms in nearly equivalent coordination environments. Throughout the **1SPER → 1Q** reaction, the hydrogen bond between O6 and the water ligand shortens and strengthens. Formation of **1Q** from **1SPER** is 9.83 kcal/mol exothermic.

The necessity of generating the catalytically active di-(μ-oxo) core of Q indicates the importance of the carboxylate shift that occurs between $H_{superoxo}$ and **1SPER**. Without the Glu243 O6 atom repositioning to form the hydrogen bond, O3 would not have been able to serve as the second bridging oxygen atom in either **1SPER** or **1Q**. Precedence for the lability of the carboxylate groups in the MMOH active site and related units has been established experimentally[42,80–83] and theoretically.[84,85]

(79) Valentine, A. M.; Tavares, P.; Pereira, A. S.; Davydov, R.; Krebs, C.; Hoffman, B. M.; Edmondson, D. E.; Huynh, B. H.; Lippard, S. J. *J. Am. Chem. Soc.* **1998**, *120*, 2190−2191.
(80) Nordlund, P.; Eklund, H. *Curr. Opin. Struct. Biol.* **1995**, *5*, 758−766.
(81) Rardin, R. L.; Tolman, W. B.; Lippard, S. J. *New J. Chem.* **1991**, *15*, 417−430.
(82) Tolman, W. B.; Liu, S. C.; Bentsen, J. G.; Lippard, S. J. *J. Am. Chem. Soc.* **1991**, *113*, 152−164.
(83) Lee, D.; Lippard, S. J. *Inorg. Chem.* **2002**, *41*, 2704−2719.
(84) Torrent, M.; Musaev, D. G.; Morokuma, K. *J. Phys. Chem. B* **2001**, *105*, 322−327.
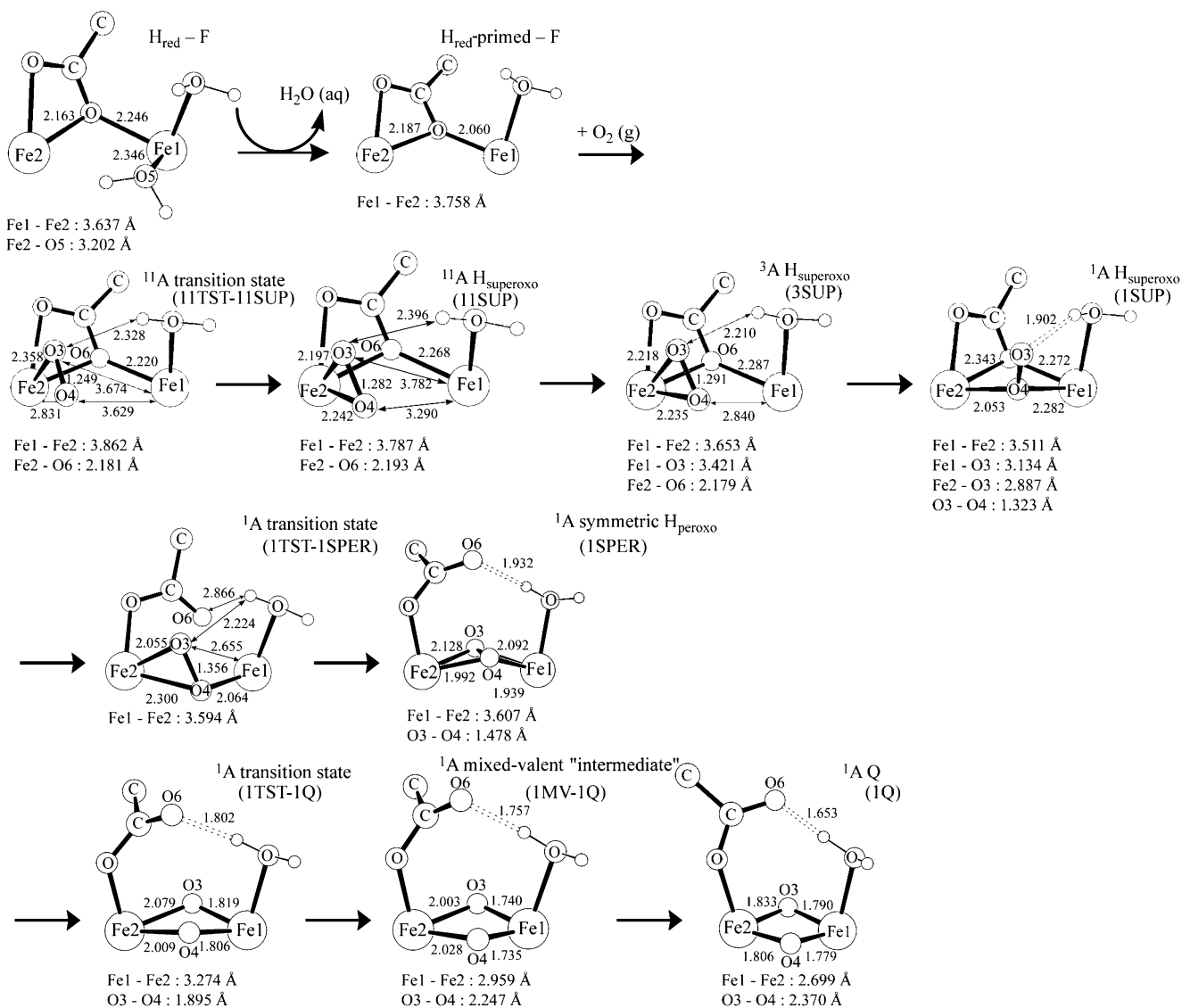
Figure 8. Detail of the proposed reaction pathway for dioxygen activation in MMOH. Cores of the minimized structures are shown. Single numbers indicate distances (Å). Dashed lines represent hydrogen bonds.

In the Fe(IV)Fe(III) mixed-valent structure, the singlet peroxide moiety originating from dioxygen has been reduced by one electron, yielding two bridging oxygen atoms which together carry a formal charge of −3 and one unpaired spin, which may be either spin up or spin down (Figure S18). The spin down case leads to an overall multiplicity of one and was just discussed in detail above. The spin up case leads to a multiplicity of 3, prompting the exploration of the triplet counterparts of **1TST-1Q** and **1MV-1Q**. These [3]A counterparts (Figure S19, Table S13) were structurally similar, but had electronic energies 24.66 and 6.21 kcal/mol higher than **1TST-1Q** and **1MV-1Q**, respectively. This result placed the [3]A surface significantly above the [1]A surface for the **1SPER → 1Q** reaction and ruled out the participation of [3]A transition states and intermediates in this reaction.

D. Comparison of Computed Free Energy Barriers with Experimental Rate Constants. From the free energy barriers determined along the optimal pathway, rate constants for each

segment of dioxygen activation can be readily computed from transition state theory (eq 1)

$$k_{obs} = (k_B T\kappa/h) \exp (-\Delta G^{\ddagger}/RT) \qquad (1)$$

where k_{obs} is the observed rate constant, $\Delta G^{\ddagger}$ is the activation barrier, k_B is Boltzmann's constant, T is temperature, κ is the transmission coefficient (taken to be approximately 1), h is Planck's constant, and R is the gas constant.

Table 4 presents the free energy barriers for the formation of each key intermediate and the associated rate constants. Conversely, experimentally determined rate constants may be translated into free energies of activation (Table 4) according to eq 2. These results are discussed further in the Discussion section below.

$$\Delta G^{\ddagger} = -RT \ln (k_{obs}h/k_B T\kappa) \qquad (2)$$

E. Calculation of Spin-Exchange Coupling Constants. The present results can be used to obtain theoretical spin-exchange coupling constants for each intermediate involved in dioxygen

(85) Baik, M. H.; Lee, D.; Friesner, R. A.; Lippard, S. J. *Isr. J. Chem.* **2001**, *41*, 173−186.

Table 4. Theoretical and Experimental Free Energies of Activation and Rate Constants for Formation of Intermediates along the Proposed Pathway for Dioxygen Activation in MMOH

	theoretical		experimental			
	total $\Delta G^{\ddagger}$ at 4 °C (kcal/mol)	rate constant at 4 °C (sec^{-1})	total $\Delta G^{\ddagger}$ at 4 °C (kcal/mol)		rate constant at 4 °C (sec^{-1})	
species formed						
H$_{superoxo}$ (11SUP)	11.44	5.50×10^3	n/a		n/a	
			with MMOB	without MMOB	with MMOB	without MMOB [45]
symmetric H$_{peroxo}$ (1SPER)	22.09	2.20×10^{-5}	15.80–16.18	19.61–19.99	1–2 [44]	0.001–0.002
			14.82–14.97	18.62–18.78	9–12 [13]	0.009–0.012
			14.41	18.22	25 [11,14]	0.025
			with MMOB	without MMOB	with MMOB	without MMOB [45]
intermediate Q (1Q)	17.86	4.77×10^{-2}	16.62	18.66	0.45 [14]	0.011
			15.70	17.73	2.4 [13]	0.060

Table 5. Energy Differences, Coupling Constants, and Singlet Stabilization Energies for HS versus BS States for Key Intermediates Involved in Dioxygen Activation in MMOH

	electronic energy difference: AF − F (kcal/mol)	J (cm^{-1})		singlet stabilization energy (kcal/mol)
species		computed	experimental value	
H$_{red}$	+0.13	+2.8	+0.35[39]	−0.03
H$_{red}$-primed	−2.13	−46.6	n/a	0.53
H$_{superoxo}$ (^{3}A, ^{11}A)	−0.13	−2.3	n/a	0.03
H$_{superoxo}$ (^{1}A, ^{9}A)	−8.22	−143.7	n/a	1.64
asymmetric H$_{peroxo}$	−0.69	−9.7	n/a	0.11
symmetric H$_{peroxo}$	−3.95	−56.0	n/a[a]	0.64
Q	−10.23	−223.6	<−30[16]	2.56

[a] Mössbauer spectra at strong fields at 4.2 K have indicated the symmetric H$_{peroxo}$ to be diamagnetic and hence AF-coupled.[11,14]

activation. Use of the BS approach to model AF states leads to spin contamination, in which the AF state generated by the procedure is actually a linear combination of spin eigenfunction determinants. Making the assumption that the two iron atoms in the MMOH system are equivalent, the magnetic coupling constant J and the stabilization energy of the pure singlet state versus the BS state can determined.[22,56,86] The relevant Heisenberg Hamiltonian (eq 3), where S_A and S_B are the spin quantum numbers for the two

$$H_{spin} = (-2J)S_A S_B \qquad (3)$$

metal centers in the high spin (HS) case and $S_A S_B$ is the operator dot product, leads to the energy difference between the HS, i.e., F-coupled, and BS states (eq 4). Using eq 4 the J values for each of the intermediates involved in dioxygen activation were determined (Table 5).

$$E_{HS} - E_{BS} = (-4J) S_A S_B \qquad (4)$$

The computed J values are in reasonable agreement with those obtained from spectroscopy.[16,39] The largest coupling constant is for intermediate Q, which is AF-coupled, has the shortest Fe−Fe distance among all the intermediates, and contains the bridging ligands most able to mediate AF-coupling. Coupling constants and energy differences between the HS and BS states are smaller for the other intermediates, consistent with their longer Fe−Fe distances and bridging ligands less optimal for spin-exchange coupling. The stabilization energy of the pure singlet compared to the BS state is equal to −4J, and is similarly computed for each intermediate (Table 5). With the generally

(86) Zhao, X. G.; Richardson, W. H.; Chen, J. L.; Li, J.; Noodleman, L.; Tsai, H. L.; Hendrickson, D. N. *Inorg. Chem.* **1997**, *36*, 1198−1217.

weak spin couplings between the iron atoms, the singlet stabilization energies are negligible. The only exception is for intermediate Q, where the calculated splitting is larger, making formation of **1Q** now exothermic by $\Delta G = -10.60$ kcal/mol versus H$_{red}$ (cf., Table 2).

Discussion

A. Comparison with Experimental Data. A.1. Existence of Intermediates Prior to H$_{peroxo}$. It has been reported that the rate of decay of reduced enzyme is more rapid (22−26 s^{-1}) than the formation of H$_{peroxo}$ (9−12 s^{-1}),[13,43] leading to the conclusion that there may be another intermediate between H$_{red}$ and H$_{peroxo}$. Our calculations, in contrast, admit only intermediates that are substantially higher in free energy than either the reactants or products. Simple modeling of the kinetics demonstrates that at room temperature these states have negligible populations and hence cannot affect the formation and decay rates as postulated above. Although population of the superoxo intermediates in Figure 7 (**11SUP**, **3SUP**, and **1SUP**) occurs quite rapidly, return to the original starting point H$_{red}$ is even more rapid (by microscopic reversibility) and the practical effect is to set up a quasi-equilibrium in which the populations of the superoxo states are proportional to the Boltzmann factors $\exp(-\beta\Delta G)$, where ΔG refers to the free energy difference between H$_{red}$ and the intermediate in question. As stated above, estimates of these Boltzmann factors at ambient temperature yield populations many orders of magnitude below 1% and hence not detectable in the experiments employed to study this reaction to date. Furthermore, observed depletion of H$_{red}$ on this time scale would be negligible as well.

At present, we do not have a theoretical explanation for the experimentally observed discrepancy between the H$_{red}$ depletion and H$_{peroxo}$ formation reported in refs 13 and 43. Reproduction of these results with our current set of intermediates would require postulating gross errors in the DFT calculations not only with regard to the energy of the superoxo intermediates, which would have to be ∼10 kcal/mol lower than the results shown in Figure 7, but also for the free energy barriers to superoxo formation. These barriers would at the same time need to be ∼10 kcal/mol *higher* than those presented in Figure 7 in order to reproduce the rate of initial depletion of H$_{red}$. Retention of the present barriers would predict that depletion would occur on a picosecond time scale. We view the conjunction of these postulated errors to be highly unlikely, particularly in view of the excellent agreement between theory and experiment for well-established kinetic and thermodynamic observations, as enumerated below. It is of course possible that there are intermediates on the potential energy surface which we have failed to identify,

despite a strenuous effort to search relevant regions of the phase space. Finally, the reported differences in experimental rate constants are quite small, and could conceivably be rationalized by alternative interpretations of the experimental data itself. Resolution of this issue awaits further experimental and theoretical investigation.

A.2. Formation of H$_{peroxo}$: Transition State and Reaction Rate Constants. The rate determining step in our model reaction occurs at the transition state **1TST-1SPER**. This transition state has an O—O bond order that is intermediate between that for superoxo and peroxo, a result that is consistent with the ^{18}O isotope effect measurements of ref 50. No proton uptake or release is required in our pathway, in contrast to suggestions made in ref 43. As in the case of the proposed intermediate between reduced enzyme and H$_{peroxo}$ discussed above, there are alternative explanations for the experimental dependence of H$_{peroxo}$ formation on pH. In particular, the results show that H$_{peroxo}$ formation diminishes substantially as the pH is raised,[43] which could be due to alterations in protein structure as a result of deprotonation of a key functional group, changing the free energy of the transition state. Alternatively, there might be a pH dependence in the K_d value for the MMOH/MMOB protein—protein complex during this step. Investigation of these or other possibilities involving structural changes of the protein is exceedingly difficult in the absence of geometric data at higher pH.

The computed free energy of activation for the formation of H$_{peroxo}$ is in good agreement (1—2 kcal/mol) with the most recent experimental data,[44] provided that these are corrected approximately for the effects of removal of protein B (MMOB).[45] In particular, in experiments with the MMO OB3b system, addition of stoichiometric concentrations of MMOB to MMOH increased the rate of reaction of H$_{red}$ with dioxygen by 1000-fold.[45] Our calculations cannot account for any effects of MMOB, but such a comparison is the most realistic at this time. Clearly, this is an area for further work, given the range of rate constants reported experimentally. From the experimental side, obtaining a crystal structure of MMOH complexed with MMOB would be very helpful in increasing the quantitative precision of the modeling effort. From the theoretical side, the use of QM/MM, rather than QM, calculations is mandated.

Our proposed H$_{peroxo}$ structure, which has a μ-η^2:η^2 peroxo coordination similar to that in refs 24 and 25, is qualitatively consistent with Mössbauer spectroscopic data that indicate nearly equivalent environments for the two iron atoms.[11,14] The thermodynamics of our H$_{peroxo}$ intermediate are consistent with appreciable population buildup of this species, allowing the observation of the spectroscopic signatures described above. This point is not trivial; making valid total energy comparisons in calculations of this type is highly challenging, requiring the use of large basis sets, accurate geometry optimization, large structural models that embody error cancellation in a consistent fashion, and exploration of a range of possible local minima in the structure. Alternative theoretical models of H$_{peroxo}$ in the literature[22-32] to date either fail to present total energies or yield results that are inconsistent with experimental observations. Previously, the similarities of the Mössbauer spectral parameters between a synthetic model and the enzyme intermediate were used to propose a cis-μ-η^1:η^1 core structure for H$_{peroxo}$,[49] which we were unable to confirm in our study. The cis-μ-η^1:η^1

structure does not afford a stable intermediate in our calculations, suggesting that the identical isomer shift of $\delta = 0.66$ mm s^{-1} observed for the (μ-1,2-peroxo)bis(μ-carboxylato)diiron(III) model complex[49] and the enzymatic intermediate is a fortuitous match. In this respect, a μ-η^2:η^2 peroxo diiron(III) synthetic model would be most valuable to obtain.

A.3. Conversion of H$_{peroxo}$ to Q. As was discussed above, our model for the conversion of H$_{peroxo}$ to Q involves homolytic cleavage of the O—O bond, rather than heterolytic cleavage as suggested elsewhere.[43] As in the case of H$_{peroxo}$ formation, we see no evidence for the involvement of protons, and found no plausible, energetically competitive pathway in which protonation might play a role. The calculated activation energy is in excellent agreement with the experimental measurements,[13,14] provided these are again corrected for the removal of protein B which slows the conversion of H$_{peroxo}$ to Q by 40-fold (Table 4).[45] The thermodynamics (Table 2) are also consistent with Q, rather than H$_{red}$ or H$_{peroxo}$, being the most stable species prior to reaction with substrate.

B. Electron Transfer. The reductive activation of dioxygen is overall a 4-electron process that transforms both oxygen atoms from their initial oxidation state of (0) to bridging oxo-ligands with formal oxidation states of (-2). Consequently, both Fe(II) centers in H$_{red}$ become formally oxidized to Fe(IV) in Q. To understand this reaction, it is necessary to identify the points on the reaction energy profile (Figure 7) where the electron transfer (ET) processes take place.

As can be expected, the first ET occurs upon initial dioxygen binding to Fe2 at the transition state **11TST-11SUP** indicated by a decrease of the spin density from 1.00 to 0.85 and 0.92 for O3 and O4, respectively (Table 3). Thus, at the transition state an equivalent of 0.23 β-electrons has been transferred from the diiron unit to the dioxygen moiety. Interestingly, the spin density of Fe2 only changes by 0.07 as a result of polarization effects that provide electron density flux from the ligands to the metal center. This first transition state is 'early' in the sense that little superoxo character is developed at **11TST-11SUP**. The O3—O4 distance changes by only 0.034 Å, from the value of 1.215 Å in free dioxygen to 1.249 Å at the transition state. An additional 0.2 β-electrons flow to the [O3—O4] moiety upon relaxation to the intermediate **11SUP**, accompanied by further lengthening of the O3—O4 distance to 1.282 Å. Clearly, the oxygen—oxygen bond becomes weaker as a result of the partial reduction, as expected, but the bidentate coordination (Figure 8) prevents the development of full superoxo character.

As described above, ISC events take **11SUP** ultimately to its analogue **1SUP** on the singlet surface (Figure 7), which is a remarkable transformation. Most notably, the bidentate binding mode of the [O3—O4] moiety to only Fe2 is no longer a stable motif and the structure rearranges to afford a geometry where O4 forms a bridge between both iron centers, whereas O3 is stabilized by a weak hydrogen bond to the axial water ligand on Fe1 (Figure 8). Spin densities of -3.75 and $+4.04$ at the AF-coupled iron centers Fe1 and Fe2, respectively, indicate an Fe1(II)/Fe2(III) mixed valence complex. In **1SUP**, the superoxo character is fully developed with an overall spin density of -0.83 on the two oxygen atoms, indicating that more than a full electron has been transferred compared to the free triplet dioxygen. Note that the sum of the spin densities on the two oxygen atoms was $+1.57$ in **11SUP**, suggesting that less than
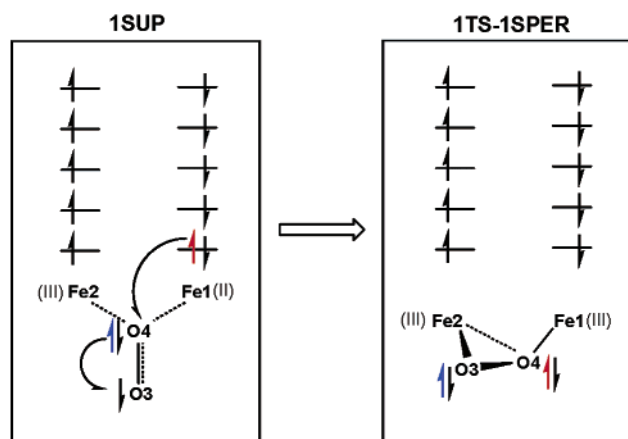
Figure 9. Schematic illustration of the proposed double exchange mechanism for the transformation **1SUP → 1TST-1SPER**.

half an equivalent of electrons were transferred. Thus, ISC plays an active role in promoting the electron transfer. The increased O3−O4 distance of 1.323 Å compared to that in **11SUP** further corroborates the formation of a true superoxo species on the singlet potential energy surface. Of importance for the next step of the reaction is the fact that the dangling oxygen (O3) in **1SUP** is the less reduced end, with a greater excess of unpaired β-electron spin density indicated by a Mulliken spin density of −0.60 compared to the bridging oxygen, which has a spin density of −0.23 (Table 3).

The next step of the reaction involves rotation of the O3-end of the superoxo group seemingly to attack Fe2, forming an Fe2−O3 bond at the transition state **1TST-1SPER**. This result is surprising because Fe1 is the less oxidized iron site with a formal oxidation state of (II), as pointed out above. Thus, the most natural path would have been oxidative attack of O3 at Fe1(II), rather than at Fe2(III). Instead, our calculations point to a double-exchange mechanism, as illustrated in Figure 9. Upon structural change, the redox active α-electron from the Fe1 center (marked in red) moves to O4, triggering in turn α-electron transfer from O4 to O3. The ET is assisted by a significant contraction of the Fe1−O4 bond, which shortens by 0.22 Å from 2.28 Å in **1SUP** to 2.06 Å in **1TST-1SPER**. At the same time, the Fe2−O4 bond is elongated to a similar extent to give an iron−oxygen distance of 2.30 Å in the transition state. A more detailed analysis of this proposed ET-mechanism will be presented elsewhere.[87] The second ET step completes with the structural relaxation of **1TST-1SPER** to give a symmetric peroxo species **1SPER** where the main electron flow takes place between Fe1 and O4 (Table 3). The spin densities also indicate that **1SPER** is a fully developed peroxo species with nearly symmetric μ_2-binding of the peroxo moiety to both iron centers that are formally in Fe(III) states.

We mention in passing that the above-described mechanism for the first two electron-transfer steps shows similarities and differences to what is proposed[65,88] for the structurally related dioxygen transport metalloprotein hemerythrin (Hr).[89] In Hr, a similar diiron core bridged by two carboxylate and one oxo ligands is observed, which can reversibly bind molecular dioxygen as a peroxo species. Unlike in H_{red}, the deoxy form

of Hr contains two AF-coupled iron centers requiring a spin flip after the first ET to allow for a spin-allowed second ET. Although our proposal for the formation of the peroxo intermediate **1SPER** also includes ISC and double exchange, the purpose of this mechanism is not to enable a spin-allowed ET. Because the two iron centers in H_{red} that function as electron donors are F-coupled, two-electron reduction of triplet dioxygen is intrinsically a spin-allowed process. It appears that the main reason for the complex ET mechanisms is to reduce the energetic requirements for the redox reaction. Unraveling the exact relationships between structural change, coupling of spin states, and the redox reaction energy is a challenging task that will be pursued in future work.

The last step of the reaction is a two-electron reduction of the peroxo group. Unlike the first half of the 4-electron reduction described above, the second half progresses without a stable mixed valence intermediate. The transition state **1TST-1Q** is characterized by an asymmetric structural distortion, where the Fe1−O3 and Fe1−O4 bonds contract significantly to 1.819 and 1.806 Å, respectively (Figure 8). Inspection of the differential spin densities between the peroxo intermediate and this transition state reveals that ET takes place to a notable extent, giving rise to increased β-electron densities at both oxygen atoms (Table 3). As expected, reduction of the peroxo group leads to further weakening of the O−O bond, which is essentially broken at the transition state with a distance of 1.895 Å. It is interesting to note that the same coupling of structural distortion with an ET event had previously been identified to play a major role in promoting the hydroxylation of methane by Q.[33,90] The mechanistic implication of this structural distortion promoting ET is distinctively different from what has been implied from experimental studies.[15] In these studies, the asymmetric 'diamond-shaped' $Fe_2(\mu\text{-}O)_2$ core structure proposed for Q was viewed as a head-to-tail dimer of Fe(IV)=O units suggesting a mechanistic resemblance between MMOH and cytochrome P-450,[91] where a single Fe(IV)=O center is found. The asymmetric structural distortion in our proposal is not only different in the sense that both contracted Fe−O bonds occur at the same iron center, whereas those at the other iron atom are elongated, but also that the $Fe_2(\mu\text{-}O)_2$ core cannot be viewed as a dimeric analogue of cytochrome P-450, where two Fe(IV)=O units carry out ET reactions relatively independent from each other. Instead, it is more appropriate to view the coupling of the structural core distortion to ET as an intrinsic feature of the $Fe_2(\mu\text{-}O)_2$ motif.[90]

The final step, formation of the catalytically competent intermediate Q by contraction of the Fe2−O3 and Fe2−O4 bonds accompanied by ET from the Fe2(III) center to the oxygen moieties, takes place without another stationary point from **1TST-1Q**. At this point on the reaction energy profile, all four electrons have been transferred to give the Fe_2O_2 core containing the oxidatively potent Fe(IV) centers linked by two bridging oxo-ligands.

C. Comparison with Alternative Computational Models. Over the past several years, there have been a substantial number of efforts to construct computational models of dioxygen activation by MMOH. We lack the space here to contrast all of

(87) Baik, M.-H.; Gherman, B. F.; Lippard, S. J.; Friesner, R. A. Unpublished results.
(88) Brunold, T. C.; Solomon, E. I. *J. Am. Chem. Soc.* **1999**, *121*, 8277−8287.
(89) Stenkamp, R. E. *Chem. Rev.* **1994**, *94*, 715−726.

(90) Baik, M. H.; Gherman, B. F.; Friesner, R. A.; Lippard, S. J. *J. Am. Chem. Soc.* **2002**, *124*, 14 608−14 615.
(91) Lipscomb, J. D.; Que, L. *J. Biol. Inorg. Chem.* **1998**, *3*, 331−336.

these models in detail with the results presented above. Key points of differentiation can be noted as follows, however.

(1) Use of Models of Adequate Size: This point is particularly important for the reduced enzyme, where we[22] and others[30−32,92,93] have noted that smaller models in the ∼60 atom range will yield, upon geometry optimization, structures for the diiron core that are grossly at variance with the experimental crystal structure. There is a nontrivial impact of model size on the quantitative energetics at other points in the catalytic cycle as well, however. Furthermore, small models are incapable of characterizing structural changes in the second coordination shell of the core, which are clearly important in stabilizing various MMOH intermediates and transition states.

(2) Quantitative Treatment of Spin: Treatment of spin should be faithful to the experimental observations and based on rigorous comparisons of the energetics of the various possible spin states. Although simplifying approximations, such as always treating the iron atoms as F-coupled, have been employed in a number of studies[23−25,30−32] to make the calculations easier, they are unnecessary when state-of-the-art computational techniques are employed. We view an accurate description of spin couplings throughout the chemical transformations as an intrinsic aspect of what it means to provide a complete picture of the reaction chemistry at an atomic level of detail. In some cases, the energy splittings of candidate spin states can be quite large (cf. Table 5),[22,94] and significant errors can arise from use of the non-optimal spin states.[24,25]

(3) Extensive Exploration of the Potential Energy Surface to Locate the Minimum Free Energy Species for Each Intermediate and Transition State: This task is very challenging for MMOH modeling if large models of the active site are used, but it is essential if the correct structures and thermodynamics for intermediates and transition states are to be produced. Our own early work[22] was deficient in this area in some respects. The structure for H_{red} presented here differs from that previously described.[22] The current model for H_{red} coordinates the water molecule trans to the histidine residues to Fe1 (Figure 4), whereas the previous model had the water molecule only weakly associated to the diiron core. The current model is in better accord with the crystallographic data[41] regarding the position of this water molecule and is lower in energy by 23.28 kcal/mol. The model for intermediate Q is also different. In the previous model, the Glu243 oxygen bound directly to Fe2 was hydrogen bonded to the water ligand on Fe1, in contrast to the current model which has the hydrogen bond from O6 in Glu243 (Figure 8). Although our previous model had key properties, including spin, charge, and Fe−Fe distance, closely comparable to those of **1Q**, the energy of our new model, **1Q,** is lower by 17.2 kcal/mol. This energy difference is partly due to the increased geometry optimization performed in this study, but the similarity of the two structures (RMS = 0.91 Å, core RMS = 0.56 Å) makes determining the exact sources of the energy difference nearly impossible based on structural examination alone. Nonetheless, the higher stability of **1Q** is key to achieving a correct overall thermodynamics for the dioxygen activation reaction. With the current model for intermediate Q (**1Q**), $\Delta G = -9.83$ kcal/mol for the **1SPER** →

1Q reaction, which is exothermic as expected. In contrast, the Q structure from ref 22 has a free energy ∼6 kcal/mol higher than **1SPER**.

Other work in the literature in general manifests similar problems, in essence, failure to locate geometries that optimize the electrostatics and hydrogen bonding energetics of the highly complex active site core structure.[24,25] This problem in turn has resulted in an inability to generate quantitative free energies for the various relevant species on the reaction path, as is discussed further below.

(4) Calculation of Quantitative Total Energies for Thermodynamics and Kinetics Which Can be Compared with Experimental Data: The reaction energy profile presented in Figure 7 agrees fairly well with the available experimental data, as discussed above. The computed free energy barriers are within the range of errors expected of hybrid DFT calculations with large basis sets, and the thermodynamics are consistent with the experimental observation of the various intermediates. Such is not the case with the preponderance of results reported in the literature to date. In some cases, relative total energies of the intermediates are not provided in a meaningful fashion, making it impossible to assess the consistency with the experimental thermodynamics or kinetics.[23,24,30−32] In other cases, there are significant quantitative discrepancies between the calculations and experiment.[25] As was noted above, much of the problem is due to difficulties in producing appropriate structures. The present work suggests that it may not be necessary to invoke external factors not included in the model, such as posited unusual features of the protein, when theory and experiment exhibit large discrepancies. Rather, good agreement with experiment can emerge naturally if a model of sufficient size and quality is employed, and if the phase space of the model is adequately explored.

Conclusions

Using a ∼100 atom model, which was determined to be the minimal size capable of faithfully reproducing the active site in the H_{red} crystal structure, and broken-symmetry unrestricted DFT quantum chemical methods, we have proposed, after thorough exploration of phase space, a multistep mechanism for dioxygen activation in MMOH taking into account energetics and spin/coupling compatibility. Following the loss of a water molecule to solution from H_{red}−F to generate H_{red}-primed−F, dioxygen reacts with H_{red}-primed−F to give an ^{11}A $H_{superoxo}$ structure. ISC then leads from the F-coupled ^{11}A $H_{superoxo}$ to the AF-coupled ^{3}A $H_{superoxo}$, which relaxes in a second ISC to the ^{1}A $H_{superoxo}$. Ensuing reaction at this point generates the ^{1}A symmetric H_{peroxo}. The peroxo intermediate then decays with homolytic cleavage of the oxygen−oxygen bond to yield intermediate Q.

Each of the intermediates and transition states has key features that play important roles in the overall dioxygen activation mechanism. The interaction of the superoxide moiety with the water molecule coordinated at Fe1 stabilizes both the ^{11}A $H_{superoxo}$ and the transition state leading to its formation. Additional stabilization of ^{11}A $H_{superoxo}$ comes from the bidentate binding of the superoxo ligand to Fe2, which is oxidized to Fe(III) while Fe1 remains ferrous. The symmetric H_{peroxo} intermediate has the peroxide moiety in a symmetric bridging

(92) Lovell, T.; Li, J.; Noodleman, L. *Inorg. Chem.* **2001**, *40*, 5251−5266.
(93) Lovell, T.; Li, J.; Noodleman, L. *Inorg. Chem.* **2001**, *40*, 5267−5278.
(94) Lovell, T.; Han, W. G.; Liu, T. Q.; Noodleman, L. *J. Am. Chem. Soc.* **2002**, *124*, 5890−5894.

nonplanar μ-η^2:η^2 (butterfly) arrangement. A carboxylate shift with Glu243 from a bridging position to hydrogen bonding to the water coordinated at Fe1 is essential to formation of the symmetric H_{peroxo} intermediate. Intermediate Q has a di-(μ-oxo) core with one bridging carboxylate group and the same hydrogen bond from Glu243 as in H_{peroxo}. Along the dioxygen activation pathway, the relative energetics of the intermediates and transition states was consistent with H_{peroxo} being the first spectroscopically detected intermediate following the decay of H_{red} and with the Mössbauer characterization of H_{peroxo}. The proposed mechanisms provide support for H_{peroxo} formation and decay being pH independent, with H_{peroxo} decay occurring through homolytic cleavage of the oxygen−oxygen bond of the peroxo moiety.

The overall quality of results obtained above demonstrate that hybrid DFT methods, in conjunction with efficient computational algorithms and hardware, now represent a powerful approach to the exploration of metalloenzyme reaction chemistry. By combining experimental and theoretical results, it is possible to build up an increasingly accurate and chemically useful picture of the catalytic cycle at an atomic level of detail. The use of mixed QM/MM methods will further enhance the quality of the computational results. Continued generation of new experimental data, in part suggested by the calculations, will lead to refinement of the models due to more and better constraints.

Supporting Information Available: Supplementary text sections A−C, Tables S1-S13, Figures S1-S19, and tables of atomic coordinates and vibrational frequencies for each intermediate and transition state structure from H_{red} to intermediate Q (PDF). This material is available free of charge via the Internet at http://pubs.acs.org.

JA036506+